Triggering Reversible Anion Redox Chemistry in O3-Type Cathode through Tuning Na/Mn Anti-Site Defects

Yang Yu[1,2#], Jicheng Zhang[1#], Rui Gao[1], Deniz Wong[3], Ke An[4], Lirong Zheng[5], Nian Zhang[6], Christian Schulz[3], and Xiangfeng Liu[1,2*]

[1] Center of Materials Science and Optoelectronics Engineering, College of Materials Science and Optoelectronic Technology, University of Chinese Academy of Sciences, Beijing 100049, P. R. China

[2] College of Sino-Danish, University of Chinese Academy of Sciences, Beijing 100049, P. R. China

[3] Department of Dynamics and Transport in Quantum Materials, Helmholtz-Zentrum Berlin für Materialien und Energie, Hahn-Meitner-Platz 1, Berlin, Germany

[4] Neutron Scattering Division, Oak Ridge National Laboratory, Oak Ridge, TN 37830, USA.

[5] Beijing Synchrotron Radiation Facility, Institute of High Energy Physics, Chinese Academy of Sciences, Beijing 100049, China

[6] Shanghai Institute of Microsystem and Information Technology, Chinese Academy of Sciences, Shanghai 200050, P. R. China

* Corresponding Author: E-mail: liuxf@ucas.ac.cn (X. L.)

The two authors contribute to this work equally.

TOC

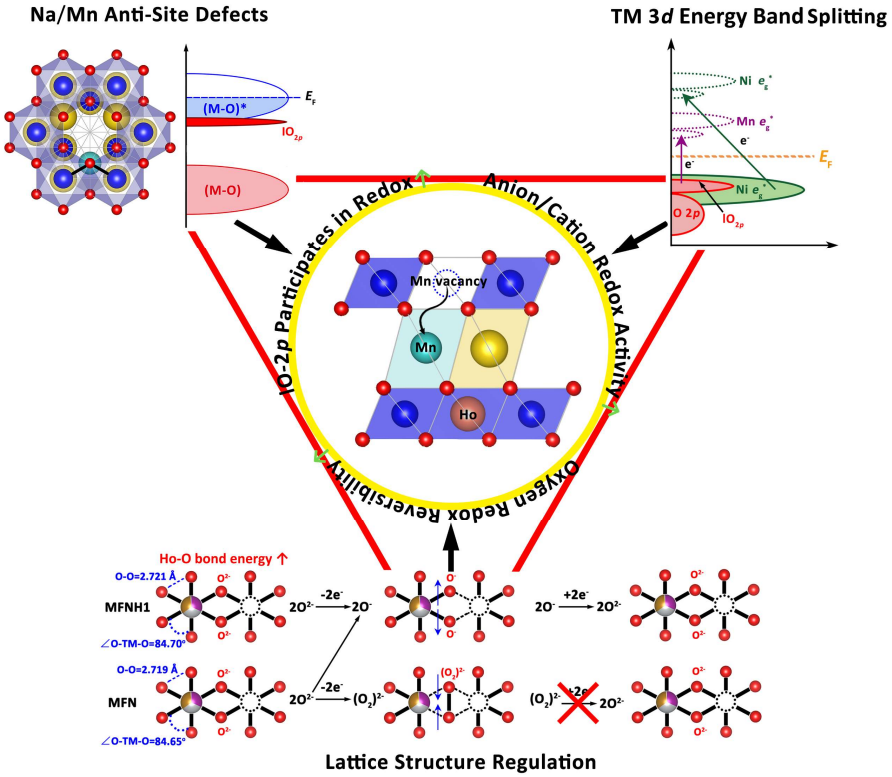
Na/Mn Anti-Site Defects
TM 3d Energy Band Splitting
(M-O)*
(M-O)
Ni
Mn
O 2p
Mn vacancy
Mn
Ho
IO-2p Participates in Redox
Anion/Cation Redox Activity
Oxygen Redox Reversibility
Ho-O bond energy ↑
MFNH1
MFN
O-O=2.721 Å
O-O=2.719 Å
∠O-TM-O=84.70°
∠O-TM-O=84.65°
-2e⁻
+2e⁻
Lattice Structure Regulation

Abstract

Oxygen anion redox (OAR) plays a crucial role on the capacity and stability of oxide cathodes in sodium-ion batteries but the intrinsic mechanism is poorly understood. How to trigger and stabilize OAR is challenging, particularly for O3-type transition metal (TM) oxide cathodes. Herein, we clarify Na/Mn anti-site defects mainly trigger OAR in O3-$NaMn_{1/3}Fe_{1/3}Ni_{1/3}O_2$ cathode, and OAR activity and reversibility can be enhanced through tuning Na/Mn anti-site defects with Ho doping. Ho^{3+} replacing Fe^{3+} site promotes more Na/Mn anti-site defects, enabling more O lone-pair electrons to participate in charge compensation. Meanwhile, Ho^{3+} enlarges O-O bond and ∠O-TM-O angle, which maintain the single-electron oxygen hole configuration of (O^-)-TM-(O^-) and inhibit O-O shortening caused by electron loss, avoiding forming $(O_2)^{2-}$ dimer. Furthermore, Ho^{3+} induces the splitting of TM 3*d* orbital energy band above Fermi level and generates low energy orbitals of Mn e_g^* and Ni e_g^*, which promotes the transition of O lone-pair electrons and Ni e_g^* orbital electrons, and simultaneously activates redox activity of anions and cations. After regulation, the capacity rises from 146.8 to 184.9 mAh g^{-1} and the capacity retention increases from 40.3 to 90.0%. This study reveals OAR mechanism in O3-type cathode and present insights on how to trigger and stabilize OAR.

Keywords

sodium-ion batteries, O3-type cathode, oxygen anion redox, Na/Mn anti-site defects, Ho doping

1. Introduction

Commercial lithium-ion batteries (LIBs) have been used in electronic device, electric vehicles and smart grids[1-5]. However, the shortage of Li resources cannot meet the rapid market demand for LIBs, and it is highly desirable to find alternatives[6-9]. Sodium-ion batteries (SIBs) have been widely studied especially for large-scale energy storage due to the rich sodium resources and the low cost. However, low specific capacity, inferior rate capability and poor cycling stability of the cathode materials hinder the practical application[10-14]. As for traditional cathode materials (both LIBs and SIBs), the charge compensation is based on the redox pairs of transition metal (TM) ions, such as $Ni^{4+}/Ni^{3+}/Ni^{2+}$, Co^{4+}/Co^{3+}, Fe^{4+}/Fe^{3+}, Cu^{3+}/Cu^{2+} and Mn^{4+}/Mn^{3+}. Energy density of the cathode is mainly limited by the content of variable valence transition metal ions. In recent years, some studies revealed that the oxygen in the lattice can also lose electrons under certain conditions which contributes an extra capacity beyond the theoretical capacity[15]. Yabuuchi et al. reported the anionic redox chemistry in a series of sodium-deficient type SIBs (P2-, P3-type, sodium content < 1) with Li^+ doping in the lattice, such as P2-$Na_{5/6}[Li_{1/4}Mn_{3/4}]O_2$[16], P3-$Na_{0.6}[Li_{0.2}Mn_{0.8}]O_2$[17, 18], P2-$Na_{0.6}[Li_{0.2}Mn_{0.8}]O_2$[19] and P2-$Na_{0.72}[Li_{0.24}Mn_{0.76}]O_2$[20]. Like lithium rich materials, the anionic redox activity of these materials is due to the existence of non-bonding O 2*p* orbits. In addition to Li^+, Yabuuchi et al. found the reversible anion redox characteristics after replacing Li^+ with Mg^{2+} doping such as P2-$Na_{0.67}[Mg_{0.28}Mn_{0.72}]O_2$[21] and P2-$Na_{0.67}[Mg_{0.33}Mn_{0.67}]O_2$[22]. Moreover, the electronic structure of Zn is $3d^{10}$, which can also activate the redox activity of lattice oxygen.

Rozier et al. reported the anionic redox activity in P2-$Na_{2/3}[Zn_{2/9}Mn_{7/9}]O_2$[23]. $Na_{4/7}[\square_{1/7}Mn_{6/7}]O_2$ ($\square$ = vacancy)[24], which directly introduces vacancies into transition metals, also has an anionic redox activity. In addition to sodium-deficient system, Mortemard de Boisse et al. also reported the anion redox in Na_2RuO_3 (sodium-rich type) whose structure is similar to that of Li_2MnO_3[25]. Recently, the oxygen anion redox (OAR) has also been reported in some other sodium-rich systems[26-28].

It should be noted that most of these studies are focused on P2-type SIBs materials. The OAR in O3-type oxides, which are regarded as the promising cathode materials[29-31], are rarely reported. If the OAR in O3-type cathode materials is activated the capacity could be further increased. In a recent study, our group reported the oxygen redox phenomenon in O3-type $NaMn_{1/3}Fe_{1/3}Ni_{1/3}O_2$ (MFN), but the intrinsic mechanism of OAR was still poorly understood[32]. In the previously reported sodium-deficient and sodium-rich oxide cathode materials, the reversible redox activity of oxygen is activated mainly due to the existence of non-bonding O 2*p* orbitals. There are two main reasons for the formation of non-bonding O 2*p* orbitals: one is the existence of alkali metal (AM) or alkaline earth metal (AEM) in the transition metal site (AM/AEM-O-Na), and the other is the vacancy defect in the transition metal site (Na-O-□). But as for conventional (non-AM/AEM system) O3-type MFN cathode, the radius of Na ion is much larger than that of transition metal ions (the radius of Na^+, Mn^{4+}, Fe^{3+} and Ni^{2+} are 1.02 Å, 0.53 Å, 0.645 Å and 0.69 Å, respectively), so it is difficult for Na^+ to enter the TM sites to form Na-O-Na structure. Therefore, what triggers OAR in O3-type MFN cathode and how to activate and stabilize OAR through a structure regulation is

challenging.

In this study, we, for the first time, based on density functional theory (DFT) calculation, clarify that Na/Mn anti-site defects, which means a fraction of Mn-ion occupy Na-ion sites leaving transition metal vacancies, trigger the OAR in O3-type $NaMn_{1/3}Fe_{1/3}Ni_{1/3}O_2$ cathode. We further propose to enhance the activity and reversibility of OAR through tuning Na/Mn anti-site defects with Ho doping. Ho^{3+} is adopted as the dopant because of large Ho^{3+} ion radius (0.901 Å), great Ho-O bond energy (627.9 kJ mol^{-1}) and strong paramagnetism. The regulation mechanism is unraveled by means of Neutron powder diffraction (NPD)[33], X-ray diffraction (XRD), X-ray absorption spectroscopy (XAS), scanning transmission electron microscope (STEM) and resonant inelastic X-ray scattering (RIXS)[34]. Ho^{3+} doping could modulate the formation of Na/Mn anti-site defects to enhance the degree of oxygen participating in the redox reaction and could adjust bond length and bond angle to improve the reversibility of oxygen redox. Simultaneously, TM *3d* orbits energy band splitting activates the redox activity of both anion and cation, and Mn pinned in Na layer enhances the crystal structural stability. In addition, the Ho-O bond with strong bond energy can inhibit the phase transition, stabilize the lattice structure and improve the redox reversibility of oxygen. After doping 0.01 mol Ho^{3+} to the Fe^{3+} site, the specific capacity increases from 146.8 to 184.9 mAh g^{-1}, and the capacity retention rate after 100 cycles at 5 C rises from 40.3% to 90.0%. This study not only reveals the intrinsic mechanism of OAR in O3-type cathode but also present some insights on how to trigger and stabilize more OAR for high-performance SIBs cathodes.

2. Results and Discussion

2.1. Characterization and Analysis of Structure

Using transition metals Mn, Fe, Ni as matrix and Ho_2O_3 as Ho source, O3-type cathode materials with different content of Ho^{3+} were synthesized by high temperature solid state synthesis ($NaMn_{1/3}Fe_{1/3}Ni_{1/3}O_2$ = MFN, $NaMn_{1/3}Fe_{1/3-0.005}Ni_{1/3}Ho_{0.005}O_2$ = MFNH0, $NaMn_{1/3}Fe_{1/3-0.01}Ni_{1/3}Ho_{0.01}O_2$ = MFNH1, $NaMn_{1/3}Fe_{1/3-0.02}Ni_{1/3}Ho_{0.02}O_2$ = MFNH2, the synthesis method is given in Supplementary Information). In order to analyze the crystal structure information of synthetic materials, NPD technique and XRD were used to characterize four groups of materials. The model for the Rietveld refinement is set according to the inductive coupled plasma mass spectrometer (ICP-MS) results of the samples. The results of ICP-MS are shown in the Table S1.

The NPD data and refinement results for MFN, MFNH0, MFNH1 and MFNH2 are presented in Figure 1(a), 1(b), 1(c) and 1(d), respectively. The XRD data and refinement results for MFN, MFNH0, MFNH1 and MFNH2 are presented in Figure S1. Different from XRD, NPD can accurately determine the position of Na element in the crystal structure of SIBs materials. Guo et al. have compared the structural characterization results of NPD and XRD of sodium ion electronic cathode materials and the result of NPD is more reliable than XRD[35]. Full-pattern Rietveld refinement is carried out using the GSAS programs with the EXPGUI interface. The refined results of NPD are shown in Table S2. The atomic occupation information of MFN, MFNH0, MFNH1 and MFNH2 are shown in Table S3, S4, S5 and S6, respectively. The refinement results of XRD are shown in Table S7. The refined results of NPD and XRD

are within the error range, and the refined results of both show that the lattice change law is the same, which can be mutually verified. All these ensure the credibility of the refined results.

By analyzing the experimental results of NPD, the following conclusions can be obtained. Firstly, in four groups of materials, each obvious diffraction peak in the patterns can be well indexed to O3-type structure with space group of $R\bar{3}m$ (no.166), indicating the α-$NaFeO_2$ phase. In addition, the NPD results of MFNH0, MFNH1 and MFNH2 do not show any observable diffraction peak of Ho_2O_3 or $NaHoO_2$, indicating that Ho^{3+} has been doped into the MO_6 lattice.

Secondly, there are Na/Mn anti-site defects in all four groups of materials (the NPD refinement results show that when the doping amount of Ho^{3+} is 0%, 0.5%, 1% and 2%, 1.34%, 1.80%, 2.07% and 2.23% defects are generated in the structure, respectively), that is, Mn ions occupy Na ion sites, leaving transition metal vacancies. It is also found that Na/Fe or Na/Ni anti-site defects do not appear in the refinement process. Furthermore, the results also show that, with the increase of doping Ho element, more Mn occupies the Na site, resulting in more Mn vacancies. The reason for this phenomenon is that Ho^{3+} ([Xe]$4f^{10}$) is rich in single electrons, it would repel the Mn ions with abundant single electrons. Therefore, the more Ho doped, the more mixed Mn cations appear in Na site.

Thirdly, with the increase of the amount of doped Ho element, the values of lattice parameters *a* and *b* gradually increase, and the value of *c* gradually decreases. The lattice parameters *a* and *b* increase because the radius (0.901 Å) of Ho^{3+} is larger than

Mn^{4+} (0.53 Å), Fe^{3+} (0.645 Å) and Ni^{2+} (0.69 Å). The decrease of *c* is because doping Ho^{3+} will promote the migration of Mn ions into the sodium layer. The radius of Mn^{2+} (0.67 Å) is smaller than Na^{+} (1.02 Å). The more Mn ions occupy the Na site, the smaller *c* is. Figure S2 is XRD diagram of normalized intensity of four groups of samples: MFN, MFNH0, MFNH1 and MFNH2. The value of intensity (003)/(104) gradually decreases with the increase of Ho doping. This comes from two main reasons. Firstly, Ho doping affects the preferred orientation of the particles, which is demonstrated by the scanning electron microscopy (SEM) images (Figure S3). Secondly, the occupation of increasing Mn into Na layer will also decrease the of (003)/(104) ratio. In addition, there is an interesting phenomenon. XRD results show that when the doping amount of Ho increases to 2%, a superstructure ordering of Na^{+}/vacancy is detected. As shown in the dotted line area in Figure S2.

Raman spectrums are shown in Figure S4. The characteristic vibration of the MFN MFNH1 and cathode at about 580 and 495 cm^{-1} belongs to a_{1g} and e_g modes, respectively. The former originates from two adjacent oxygen layers moving against each other along the *c*-axis, whereas the latter roots from the atomic displacements along the *a*-*b* plane direction. Comparing MFN and MFNH1, the peak at 575 cm^{-1} shifts to 585 cm^{-1}, which is attributed to the strengthening of force between the transition metal layer and sodium layer upon the increase of Na/Mn anti-site defects. The peak at 490 cm^{-1} shifts to 500 cm^{-1} which is caused by the expansion of the *a*-*b* plane. These results coincide well with the NPD refinement results[36].

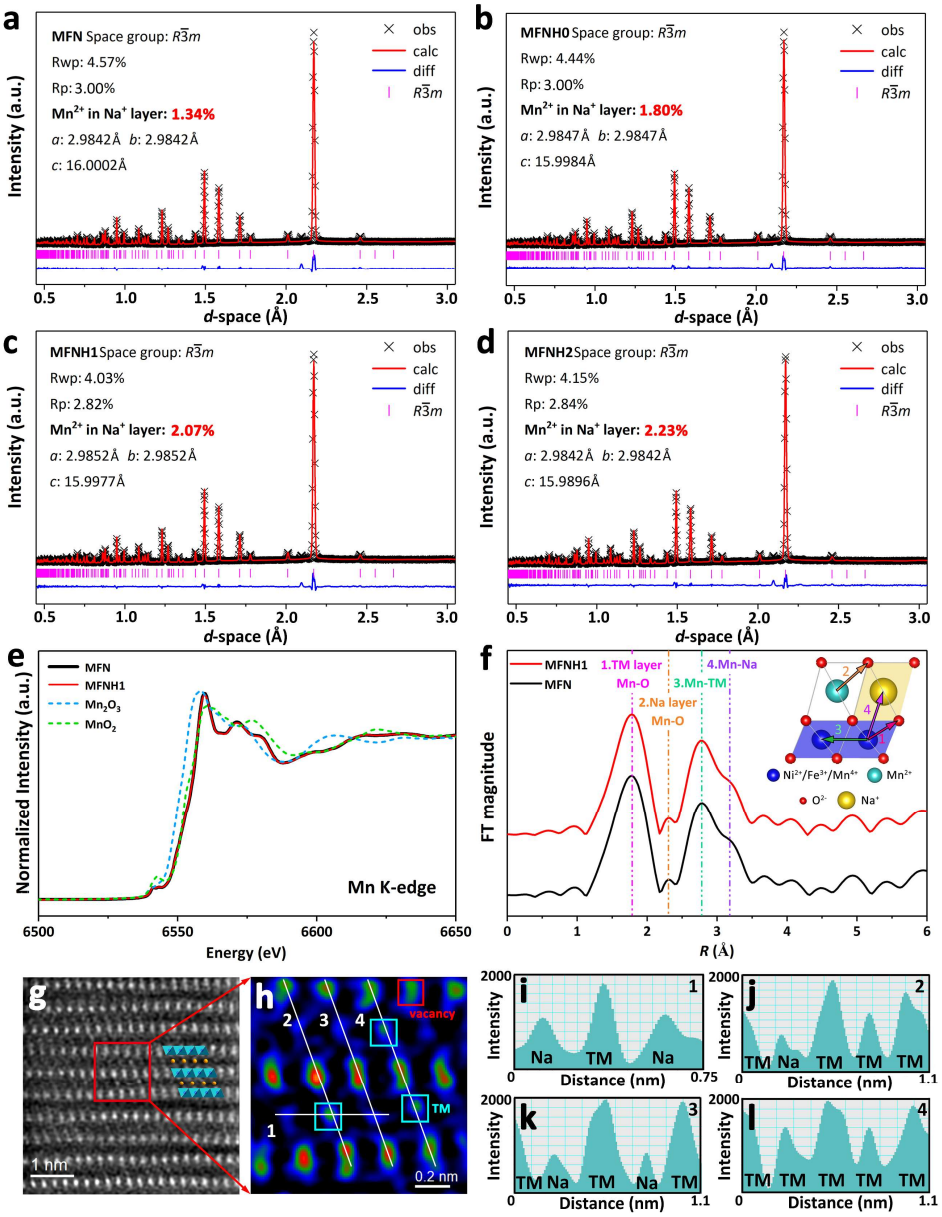

Figure 1. NPD refinement results of (a) MFN, (b) MFNH0, (c) MFNH1, (d) MFNH2. (e) XANES spectra at Mn K-edge of MFN and MFNH1. (f) Corresponding EXAFS spectra at Mn K-edge of MFN and MFNH1. (g) The atomic lattice diagram of MFNH1, along [100] zone axis, characterized by STEM. (h) The enlarged view of the red rectangle area of (g). (i), (j), (k) and (l) shows intensity diagrams of atomic sections along the directions of 1, 2, 3 and 4 from (h), respectively.

Figure S5 is the XPS results of Mn 2*p* and 3*s* orbits of the MFN and MFNH1 powder, etched to 15 nm. The results show that a small amount of Mn^{2+} ions appear in

the materials. According to previous reports, in MFN cathode, Mn ion exists in the form of Mn^{4+} in MnO_6 (TM layer)[32]. This difference may be related to our use of MnO (*Fm-3m*) as a manganese source. In most studies, the raw material of Mn used to prepare Na-ion cathode is Mn_2O_3, while here we use MnO. Due to the atomic arrangement of Mn for MnO, Mn^{2+} need to overcome the migration energy to form the TM layered oxide. And some of the Mn that fail to migrate eventually form the mixed Mn^{2+} cations occupied in Na site. And for the requirement of charge balance, some O defects are simultaneously generated. This is supported by the Electron paramagnetic resonance spectroscopy (EPR) results and NPD refinement in the following. Therefore, we infer that the detected Mn^{2+} exists in the Na layer, due to a closer radius between Mn^{2+} (0.83 Å) and Na^{+} (1.02 Å), both of which are larger than that of Mn^{4+} (0.53 Å).

XAS can characterize the coordination of transition metals[37]. Hence, the Mn K-edge XAS of MFN and MFNH1 materials were measured to characterize the structure of Na/Mn anti-site defects. XANES spectrums at Mn K-edge region of MFN and MFNH1 are shown in Figure 1(e). The results show that Mn mainly exist with +4 valence in the two materials. EXAFS spectrums in R-space at Mn K-edge of MFN and MFNH1, as shown in Figure 1(f). After the R-space analysis with Artemis software, it is concluded that the coordination of Mn mainly has four shells, namely Mn-O (TM layer), Mn-O (Na layer), Mn-TM and Mn-Na. The R-space and q-space fitting results of MFN and MFNH1 are shown in Figure S6 and S7, respectively. Four paths were added to fit R-space. In MFN, the coordination number N of the second path (Mn-O Na layer) is 5.49, and R factor is 0.0138. In MFNH1, N = 5.16, R factor = 0.0115. It shows

that the atomic coordination number of Mn's second shell should be 6, and the fitting result is within the error range. It is reported that second Mn-O peak is attributed by the Mn-O (Na layer) coordination shell which is caused by the disordered Mn cations[38]. It declares that there is a small amount of Mn in the Na layers. The fitting results are consistent with the bond length results obtained by NPD refinement. However, the occupation of Mn in Na site promotes the precipitation of Na. Therefore, a large occupation of Mn in Na site is not conducive to the performance of the cathode materials.

The XANES spectra at Fe K-edge of MFN and MFNH1 is shown in Figure S8, this shows that Fe is mainly +3 valence state. The XANES spectra at Ni K-edge of MFN and MFNH1 is shown in Figure S9, which shows that Ni mainly exist with +2 valence in the two materials. The XANES spectra at Ho L_3-edge of MFNH1 is shown in Figure S10. The R-space transformation of EXAFS spectra of Fe K-edge, Ni K-edge and Ho L_3-edge for MFN or MFNH1 are shown in Figure S11. The results show that there is no second TM-O (Na layer) coordination shell in the coordination environment of Ni, Fe and Ho, which is consistent with the results of NPD refinement. In addition, the first coordination shell information of Ho reflects that Ho occupies the site of transition metal, which proves that Ho is successfully doped into the lattice and occupied the transition metal site instead of Na site.

Explanations on why Ho occupies the TM site and Mn occupies the Na site are provided. The occupation of the doped element is not only determined by its ionic radius, but also by the valence state, bond energy and other factors. Although the ionic

radius of Ho^{3+} (0.901 Å) is closer to Na^{+} (1.02 Å) than Mn^{2+} (0.83 Å), Mn^{2+} is closer to Na^{+} from the perspective of valence state. In addition, Mn-O bond energy (402 kJ mol^{-1}) is smaller than Ho-O bond energy (627.9 kJ mol^{-1}). The bond length (~1.9 Å) of Ho-O at the transition metal layers meets the conditions for covalent bond formation. The occupation of Ho in the transition metal site increases the structural stability of the cathode by forming Ho-O bonds with large bond energy. But when Ho is in Na site, the ionic property of Ho-O bond is increased due to the elongated bond length (~2.4 Å). This reduces the Ho-O bond energy and weakens the functions of Ho in stabilizing structure. However, Mn-O bond has a small bond energy and has a reduced effect on enhancing the structural stability than Ho. In the process of synthesis, the material tends to form the most stable structure. Therefore, compared with the location of Ho at Na site, the location of Mn at Na site is more conducive to the structural stability of the material.

In order to characterize the Na/Mn anti-site defects structural phenomenon more intuitively, MFNH1 samples were characterized by STEM. Figure 1(g) shows the atomic lattice diagram, along [100] zone axis. Figure 1(h) is an enlarged view of the red rectangle area of Figure 1(g). In Figure 1(h), the red rectangle area shows the vacancy in the transition metal layer, and the blue rectangle area shows the transition metal ions migrating to the Na site. The intensity diagrams of atomic sections are made along the directions of 1, 2, 3 and 4, respectively. The intensity diagrams of atomic sections along directions of 1, 2, 3 and 4 is shown in Figure 1(i), 1(j), 1(k) and 1(l), respectively. It can be clearly seen that the transition metal ions have migrated to the

Na site, and the transition metal vacancy formed. The result from the STEM image is consistent with that of NPD refinement and XAS results. High resolution-transmission electron microscopy (HR-TEM) results (Figure S12, S13, S14 and S15) declare that no coating is formed in the Ho doped materials. The selected area electron diffraction (SAED) demonstrates only one clear set of spots for $R\bar{3}m$ space group. The results of transmission electron microscopy-energy dispersive spectrometer (TEM-EDS) and line scanning show that all elements are uniformly distributed in the lattice, and Ho elements do not aggregate on the surface to form Ho_2O_3 or $NaHoO_2$. These data support that Ho element is successfully doped into the lattice. We attribute the successful implementation of Ho doping to the following points. Firstly, the doping amount is small, which is only 1-2%. Secondly, our materials have some structural defects, which have been proved by the neutron diffraction and EXAFS. The structural defects can largely increase a material's ability to dissolve heterogeneous elements[39, 40]. This is the most important reason why Ho can be doped into transition metal sites.

2.2. Revealing the Redox Mechanism of Oxygen

In order to study the oxygen redox mechanism for O3-type transition metal-based SIBs, the O3-type MFN cathode material with Na/Mn anti-site defects crystal structure diagram was constructed, shown in Figure 2(a). Both Na and TM atoms occupy the center of oxygen octahedron, which are arranged in the way of ABCABC. As shown in Figure 2(a), there is a Na/Mn anti-site defect in the designed MFN crystal structure, that is, a Mn ion occupies a Na site, leaving a transition metal vacancy.

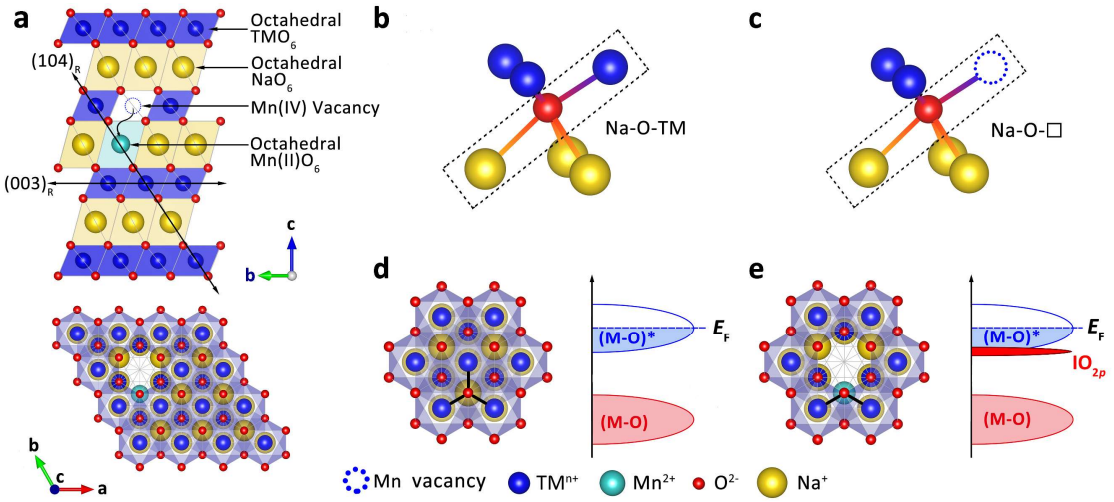

Figure 2. (a) The crystal structure diagram of MFN with Na/Mn anti-site defect. (b) The structural diagram of the Na-O-TM bonding mode in traditional O3-type cathode. (c) The structural diagram of the Na-O-□ bonding mode in O3-type MFN with Na/Mn anti-site defect. (d) The crystal structure and Fermi level diagram of traditional O3-type cathode. (e) The crystal structure and Fermi level diagram of O3-type MFN cathode with Na/Mn anti-site defect.

For traditional O3-type SIBs cathode (O/TM = 2), when octahedral coordination occurs, the extranuclear electrons of O undergo hybridization, and six electrons participate in bonding. After bonding, the energy band of O can be divided into a pair of 2*s* energy bands and three pairs of 2*p* energy bands. Since the 2*s* energy band is far away from the Fermi level (E_F), it has no electrochemical activity. The 2*p* energy band with a higher energy participates in the formation of M-O bond. The bonding mode of Na-O-TM in traditional O3-type cathode is shown in the Figure 2(b), and the structure and Fermi level diagram of traditional O3-type cathode are shown in the Figure 2(d). Near the E_F surface, there are two main energy bands from low energy to high energy: the (M-O) band of bonding state M-O, and the (M-O)* band of anti-bonding state M-O. The redox in the electrochemical process is mainly contained in the (M-O)* energy

band[41].

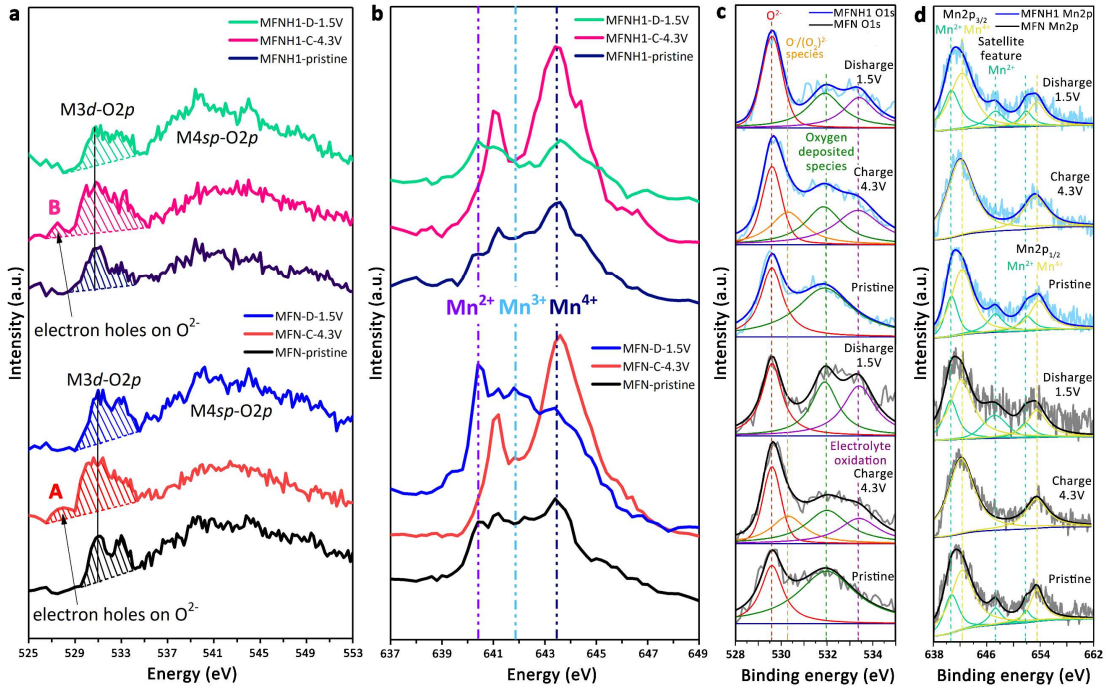

Figure 3. (a) Ex-situ soft XAS of O K-edge for MFN and MFNH1 at different voltage states. (b) Under different voltage states, MFN and MFNH1 soft XAS of Mn L-edge. (c) Ex-situ O 1*s* XPS spectrum of MFN and MFNH1, during charging-discharging process, etched to 15 nm. (d) Ex-situ Mn 2*p* XPS of MFN and MFNH1, during charging-discharging process, etched to 15 nm.

In O3-type MFN, due to the existence of Na/Mn anti-site defect, a unique Na-O-□ structure is formed. Therefore, one of the O 2*p* orbitals is not bonded, as shown in Figure 2(c). The non-bonding O 2*p* orbital has a high electron energy, and its energy band (lO_{2p}) is above the bonding state (M-O) energy band, as shown in Figure 2(e). Oxygen non-bonding state is the second energy band that can provide charge compensation on the premise of maintaining the basic stability of the structure in addition to the anti-bonding state (M-O)* energy band. As for the traditional O3-type cathode without oxygen non-bonding state energy band, once the electrons in the anti-

bonding state (M-O)* energy band are exhausted, the additional electrons can only come from the bonding state (M-O) energy band, and the participation of these energy bands will affect the structural stability of the material[42, 43]. Therefore, in theory, O3-type cathode materials with Na/Mn anti-site defects can undergo reversible oxygen redox reaction.

To study the redox mechanism of oxygen in MFN and MFNH1, ex-situ soft XAS of two materials were collected in the O K-edge region and Mn L-edge region, as shown in Figure 3(a) and 3(b). In Figure 3(a), the peak before 534 eV reflects the information of M 3*d*-O 2*p* hybrid orbit, and the peak after 534 eV reflects the information of M 4*sp*-O 2*p* hybrid orbit. The 3*d* band pre-edge peak at ≈ 531 eV (black line) shifts to a lower energy when charging to 4.3 V, which is attributed to the oxidation of TM ions[44]. Small peaks appeared before 529 eV (peak A and B), both in MFN and MFNH1 samples, when charging to 4.3 V. These peaks reflect the information of electron holes in O^{2-}, and is the evidence of oxygen oxidation reaction[45]. The integrated intensity of low energy peaks with different charge states can supply important information about the unoccupied hole states of the oxygen 2*p* orbitals, was previously verified with soft XAS by Bruce et al.[46] The integrated intensity of the pre-edge peak is calculated between 525 and 534 eV (the shaded region), and the results are shown in Figure S16. The integral area results show that MFNH1 has stronger oxygen redox activity and stronger reversibility than MFN.

In Figure 3(b), the results show that, at initial state, most of the Mn ions exist in the form of +4 valence in the two samples, and there is a small amount of Mn^{2+} but no

Mn^{3+} observed. This is consistent with the above-mentioned existence of Mn^{2+} in the Na layer. When charged to 4.3 V, Mn^{2+} in MFN is mainly oxidized to Mn^{4+} and a few to Mn^{3+}. In MFNH1, all Mn^{2+} is oxidized to Mn^{4+}. When discharged to 1.5 V, Mn^{3+} and Mn^{2+} co-exist in MFN, indicating that Mn^{2+} in Na layer will change from Mn^{2+} to Mn^{4+} and finally return to Mn^{2+} during charge and discharge, but the reaction is not completely reversible in. While in MFNH1, the redox of Mn^{2+} is completely reversible, which shows that in MFNH1, the structure of Na/Mn anti-site defects is more stable. The stability of the defects structure ensures the reversibility of oxygen redox. After doping with Ho, the average bond length of Na-O (Mn-O in Na layer) becomes shorter, indicating the lattice structure strength is higher, which may be the reason for the more stable Na/Mn anti-site defects. In addition, it is demonstrated by the Fe L-edge XAS spectra that the electronic structure of Fe changes a little for charging the pristine electrodes to 4.3 V charged electrodes (Figure S17). This demonstrates a low participation of Fe into the redox[47]. This is consistent with other work[48].

Figure 3(c) shows XPS result of MFN and MFNH1 in O 1*s* energy region after etching 15 nm. The results show a new peak of $O^-/(O_2)^{2-}$ at about 530.3 eV appears when charged to 4.3 V, indicating that oxygen participates in redox. Figure 3(d) shows Mn 2*p* XPS at the same condition. The results show that Mn^{2+} will change to Mn^{4+} when charged to 4.3 V and back to Mn^{2+} when discharged to 1.5 V, which is consistent with results of soft XAS. It proves that oxygen will participate in redox during charge and discharge, and Mn^{2+} pinned in Na layer will oxidize to Mn^{4+} and finally change back to Mn^{2+}. Since the reduction of Ar^+ etching may interfere with the results, here we

compare the spectra of the electrodes before and after etching to confirm that the signal of Mn^{2+} is indeed from the nature of the materials. The surface data of Mn, C, O XPS spectra for the electrodes before and after etching are consistent, as shown in Figure S18. This indicates that the actual binding energies of C/O do not change after etching the electrodes within 15 nm, which excludes the possibility that Mn^{2+} is produced by reduction caused by Ar^{+} etching.

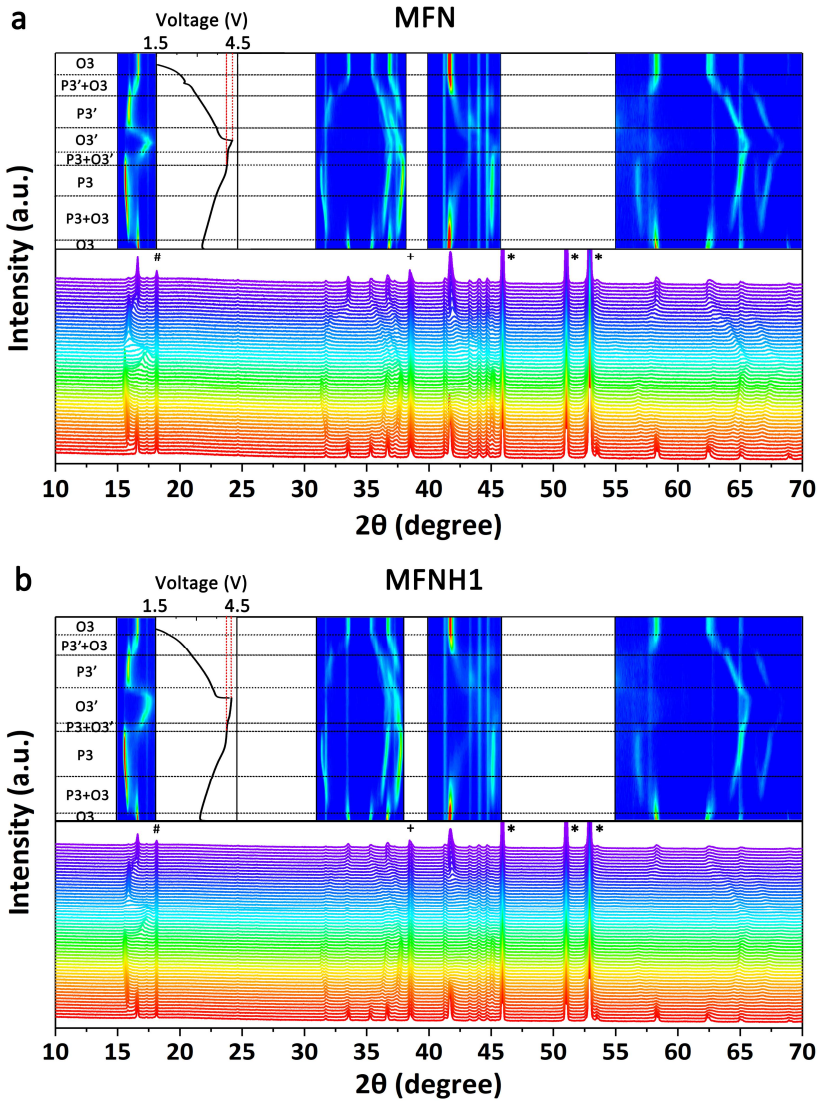

Figure 4. (a) In-situ XRD of MFN. (b) In-situ XRD of MFNH1. "#" is the peak of PTFE, "+" is the peak of Al, "*" is the peak of Be.

In-situ XRD experiments were carried out on MFN and MFNH1. The results are shown in Figure 4(a) and 4(b). Both materials experienced the transition from O3 phase to P3+O3 phase, then to P3 phase, then to P3+O3' phase, and finally to O3' phase during charging. The discharge process is an opposite process.[48] There are mainly two points deserve to be noted. Firstly, a lower peak shift for MFNH1 (0.78°) than MFN (0.82°) is showed by the main peak (003) when charging the pristine electrode to 4.3 V charged state. This illustrates that, compared with MFN, MFNH1 has a restrained structural shrinkage upon extracting Na^+ from the lattice. This would facilitate the Na^+ diffusion of MFNH1 at high voltages. Secondly, O3' phase is maintained for a longer time for MFNH1 than MFN. This is due to the pinning effect of Mn, which retards the phase transition. This helps a more oxygen participate in the redox reactions[49]. In addition, a few recent studies have shown that strong M-O bond energy plays an important role in inhibiting phase transition and stabilizing lattice structure[50, 51]. Therefore, the Ho-O bond with strong bond energy can also reduce the damage caused by phase transition and maintain the structural integrity. (The bond energy of Ho-O = 627.9 kJ mol^{-1}, Ni-O = 391.6 kJ mol^{-1}, Fe-O = 409 kJ mol^{-1}, Mn-O = 402 kJ mol^{-1}).

Yang et al. pointed out that it is not rigorous to use O K-edge XAS to characterize the redox of O[52]. Therefore, RIXS was used to characterize the oxygen redox reaction of MFN and MFNH1 materials, which can support the results of soft XAS and explain the mechanism of oxygen redox process. RIXS is a technique with a probing depth of about 100 nm at the O K range[52], has sensitivity to the oxidation state of oxygen[53], and can characterize the redox process of lattice oxygen. Ex-situ O K-edge RIXS results for

MFN and MFNH1 are shown in Figure 5(a) and 5(b), respectively. The incident energy of RIXS is 531 eV, which corresponds to an elastic peak at the energy loss of 0 eV. The energy loss spectrum of RIXS can be divided into four regions: (A) elastic peak region, (B) O-O dimer oscillation peak region, (C) the region of electronic structure of the metallic band of the oxides, which can reflect the octahedral information of TM-O hybridization, and (D) O 2*p* orbitals electron's information region. The peak of about 523.5 eV (energy loss of 7.5 eV) in D region is the fingerprint peak of oxygen oxidation reaction due to electron loss in O 2*p*[54]. In MFN and MFNH1 samples, these peaks appear when charged to 4.3 V, indicating that oxygen oxidation reaction will occur in both groups of materials, which is consistent with the results of XAS and XPS. The peak in C region can reflect the octahedral information of TM-O hybridization. In MFN sample, the peak shifted significantly to the right in the discharge state compared with the initial state, indicating that the irreversible structural change of MO_6 occurred. In MFNH1 sample, there is no obvious peak shifting between the discharge state and initial state, indicating that there is no irreversible MO_6 distortion. Region B reflects the frequency information of vibration between adjacent oxygen atoms caused by energy loss[45], and the morphology of dimer formed by two oxygen atoms can be determined. Figure 5(c) and 5(d) are enlarged views of region B in Figure 5(a) and 5(b), respectively. RIXS results of B region of MFN and MFNH1 showed that weak oscillation occurred when charging to 4.3 V, indicating that the bond length of O-O bond of the two groups of materials would change due to the loss of electrons. Judging from the oscillation frequency, O_2 molecules will not be generated, but it is difficult to judge the

morphology of O-O dimer[45]. In addition, when being discharged to 1.5 V, the oscillation peaks disappear in MFNH1 sample, while there are still oscillation peaks in MFN sample (blue dashed rectangular area). It shows that there is irreversible redox in MFN, which is consistent with the DFT theoretical calculation and O K-edge XAS results. The integral area of the elastic peak in region A reflects the density of oxygen holes. The integral area results are shown in Figure S19, which indicates that the degree of oxygen participation in the redox reaction in MFNH1 is higher[55, 56].

To further explore the redox mechanism of oxygen in the electrochemical process, DEMS and Raman spectrum testing were carried out. DEMS can on-line monitor the gas produced on cathode during charging and discharging. As shown in Figure 5(e) and 5(f), besides a small amount of CO_2 under high voltage, no O_2 is detected during discharge/charge process as for MFN and MFNH1.

Ex-situ Raman spectrum testing results of MFN and MFNH1 are shown in Figure S20 and S21, respectively. Raman spectrum can detect the O-O stretch information in bulk structure of the materials. The O-O stretch at about 850 cm^{-1} is ascribed to peroxide related $(O_2)^{2-}$ species, and at about 1150 cm^{-1} is ascribed to superoxide related $(O_2)^{-}$ species[57, 58]. Raman results show that when MFN is charged to 4.3 V, it will generate peroxide related $(O_2)^{2-}$ species, and not generate superoxide related $(O_2)^{-}$ species. When being discharged to 1.5 V, $(O_2)^{2-}$ species still exist. MFNH1 will not generate peroxide related $(O_2)^{2-}$ species or superoxide related $(O_2)^{-}$ species during charging and discharging. In addition, it should be added that, not all ex-situ Raman spectrum results (charging to 4.3 V state and discharging to1.5 V state) can detect peroxide generation.

This shows that the generation of peroxide related $(O_2)^{2-}$ species is random, and the redox of peroxide related $(O_2)^{2-}$ species is not completely irreversible.

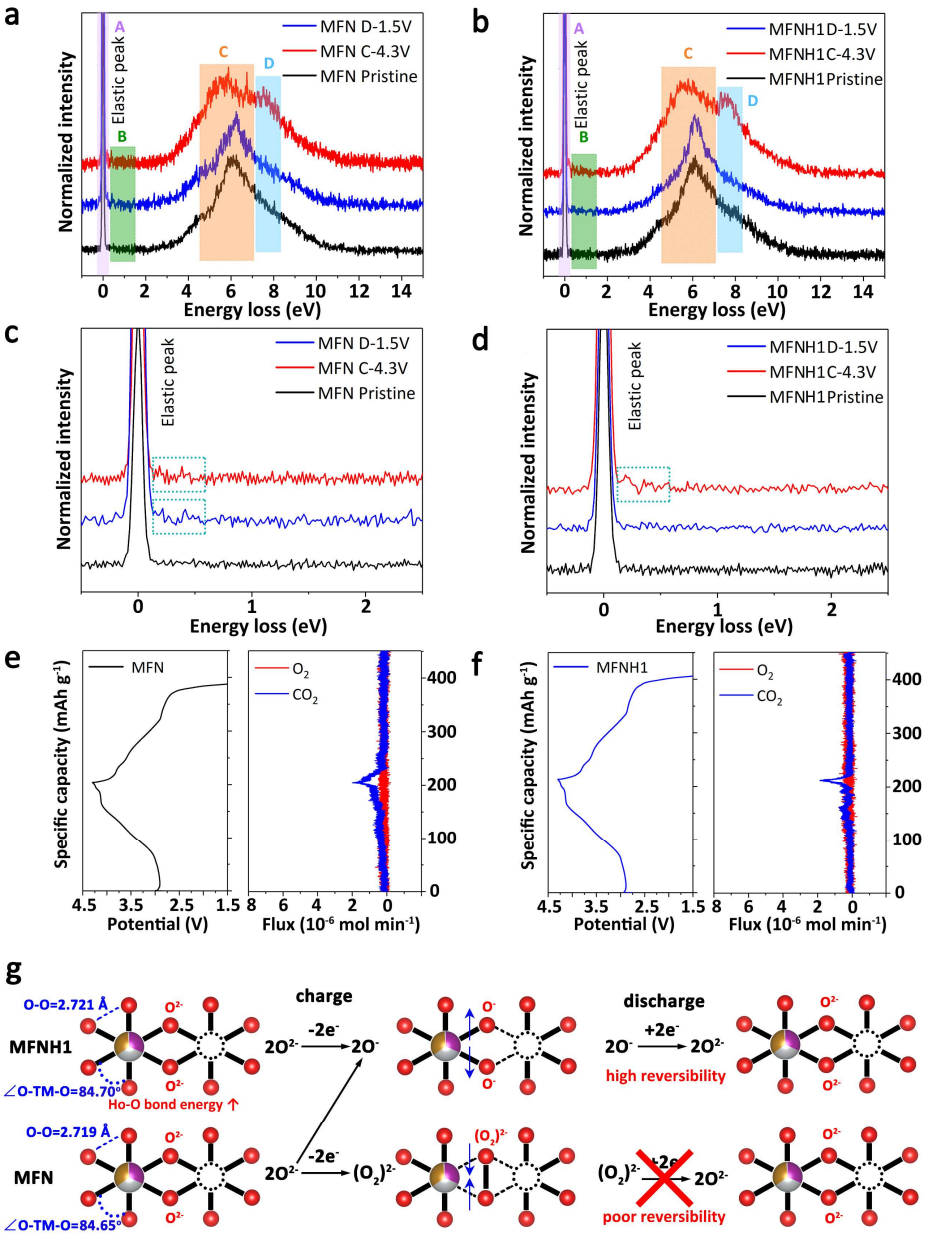

Figure 5. Ex-situ O K-edge RIXS results for (a) MFN and (b) MFNH1. (c) and (d) are enlarged views of region B in (a) and (b). DEMS results of (e) MFN and (f) MFNH1. (g) Schematic diagram of oxygen oxidation reaction process in MFNH1 and MFN materials.

EPR is also conducted. As shown in Figure S22, both samples have signals at g =

2.0. This can be explained by the anti-site defect and O defect. EPR results show that there are more anti-site defects and O unpaired electrons in pristine MFNH1, which makes the EPR signal stronger. For MFN in charging process, the signal at 2.0 in g gradually weakens, and finally almost disappears at 4.3 V. This is because O^{2-} loses electrons and forms a dimer structure at 4.3 V, which largely reduces the unpaired electrons in O. While for MFNH1, with charging the electrodes to 4.3 V, the signal at 2.0 in g still exists, which indicates an inhibition in forming O-O dimers. This result is consistent with the RIXS and Raman results.

According to the experimental results of RIXS, XAS, Raman spectra and EPR, the redox process of oxygen in MFN and MFNH1 materials are revealed. When the MFN material is charged to 4.3 V, O^{2-} will undergo oxidation reaction and generate oxygen electron holes O^- and peroxide related $(O_2)^{2-}$ species at the same time ($2O^{2-} - 2e^- = 2O^-$, $2O^{2-} - 2e^- = (O_2)^{2-}$). The redox reversibility of $(O_2)^{2-}$ species is poor. When being discharged to 1.5 V, O^- will undergo a reduction reaction and change back to O^{2-} ($2O^- + 2e^- = 2O^{2-}$), while $(O_2)^{2-}$ will not completely change back to O^{2-}. This is the reason why the soft XAS results show that the reversibility of MFN redox reaction is poor. Different from MFN, MFNH1 will mainly generate O^- which has redox reversibility, during charge and discharge, and reversible redox reaction of oxygen can occur ($2O^{2-} - 2e^- = 2O^-$, $2O^- + 2e^- = 2O^{2-}$)[56, 59]. The schematic diagram of oxygen oxidation reaction is shown in Figure 5(g). The reason why the oxidation reaction of oxygen in MFN1 will not produce $(O_2)^{2-}$ is that Ho doping changes the lattice structure. After doping Ho, the O-O bond becomes longer and the angle ∠O-TM-O becomes larger, which is

conducive to maintaining single electron oxygen hole configuration of (O^-)-TM-(O^-) and avoiding the shortening of O-O bond caused by electron loss, which could form $(O_2)^{2-}$ dimer structure with poor reversibility. Meanwhile, the Ho-O bond with a strong bond energy can stabilize the (O^-)-TM-(O^-) structure. Stable lattice structure can also avoid the formation of irreversible O-O dimers.

2.3. Electrochemical Performance

In order to compare the electrochemical properties of the materials before and after modification, the electrochemical properties of MFN and MFNH1 were tested. The assembly method of the cells is given in the Supplementary Information. Comparing the electrochemical properties of MFN, MFNH0, MFNH1 and MFNH2, MFNH1 has the best performance, shown in Figure S23 and S24. Therefore, MFNH1 was used to as the experimental group and MFN as the blank group. Figure S25 shows the first charge-discharge curves of MFN and MFNH1. The results show that the voltage platform in the voltage range from 4.1 V to 4.3 V corresponds to the oxidation reaction of oxygen[32]. In MFN material, oxygen will contribute about 35 mAh g^{-1} during charging and 19 mAh g^{-1} during discharging. This is because during the first cycle of charging, the surface oxygen will also participate in the reaction and is irreversible, which will lose part of the capacity. Therefore, it is generally believed that 19 mAh g^{-1} is the capacity provided by lattice oxygen. In MFNH1, the capacity provided by oxygen during charging and discharging is 47 and 31 mAh g^{-1}, respectively. So, lattice oxygen will provide about capacity of 31 mAh g^{-1}. According to the content of Na/Mn anti-site defects obtained from NPD refinement results, the capacity provided by oxygen redox

in MFN and MFNH1 is calculated.

One vacancy in TM layer can form 6 linear Na-O-□ structures, which provide 6 active electrons in O. These active electrons induce the O redox. And MFN has a defect content of 1.34%, while MFNH1 has a defect content of 2.07%. Based on the contents of defect, the number of active electrons is about 0.080 mol for MFN and 0.124 mol for MFNH1, which corresponds to a capacity of about 20 mAh g^{-1} for MFN and about 30 mAh g^{-1} for MFNH1 (Theoretical capacity C_0 = 26.8 Ah mol^{-1}; Molar mass M_{MFN} = 111.48 g mol^{-1}). This is consistent with the electrochemical properties experimental results. In addition, the transition metal provides a capacity of about 140 mAh g^{-1} in MFN, while MFNH1 can provide the capacity of about 160 mAh g^{-1}, indicating that the redox activity of the transition metal has also been enhanced.

The initial Coulombic efficiency of MFN and MFNH1 are calculated to be 85.5% and 88.5%, respectively. It is found that the Coulombic efficiency is higher for MFNH1 than MFN. It can conclude that the higher capacity of MFNH1 is stable, which is not from the irreversible electrolyte decomposition. The content of transition metals in the electrolyte after cycling (50 cycles at 1 C) were tested by ICP-MS. The results showed that the metal contents in the electrolyte are a little higher for cycled MFN cell (1.77 mg ml^{-1}) than cycled MFNH1 cell (1.74 mg ml^{-1}).

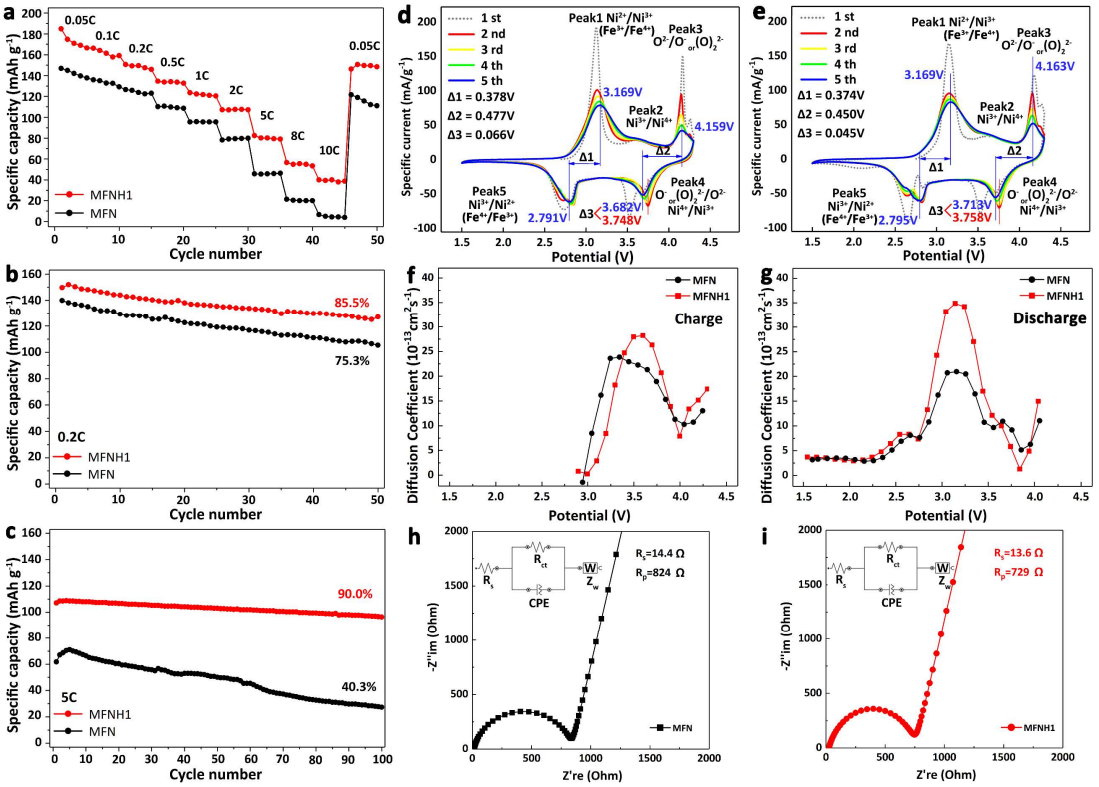

Figure 6. MFN and MFNH1 (a) rate performance diagram, (b) cycle performance diagram at 0.2 C and (c) cycle performance diagram at 5 C. CV curves of (d) MFN and (e) MFNH1 in the voltage range of 4.3 V-1.5 V. PITT curves of MFN and MFNH1 in the (f) charging process and (g) discharging process. EIS curves of (h) MFN and (i) MFNH1.

The rate performance of MFN and MFNH1 is shown in Figure 6(a), and the cycle performance results at low and high rate are shown in Figure 6(b) and 6(c), respectively. The results show that, after doping with Ho, the specific capacity increases nearly 40 mAh g^{-1}, and the rate properties are improved in different current densities from low to high. There is still 45 mAh g^{-1} specific capacity at 10 C. The cycle performance at low and high rate has been improved. Especially at 5 C, after 100 cycles, the capacity retention rate of MFNH1 sample is 90.0%, but the capacity retention of MFN sample is only 40.3%. The increase of specific capacity and the improvement of rate

performance are mainly due to the formation of more Na/Mn anti-site defects after Ho doping, which makes more oxygen participate in the capacity contribution. At the same time, Mn e_g^* energy level splitting can activate the redox activity of cation and anion at the same time. This point will be discussed later in the theoretical calculation. The enhancement of cycle stability is mainly due to the stabilization of oxygen redox reaction by Ho doping, the pinning effect of Mn^{2+} and the strong Ho-O bond inhibit excessive phase transition and stabilize the crystal structure. The lattice parameters of MFN and MFNH1 cathode materials after 200 cycles at 0.1 C are shown in Table S8, which are obtained by XRD refinement. The results show that the lattice parameters of MFNH1 material change less which indicates that the lattice strain of MFNH1 material is small.

Cyclic voltammetry (CV) curves of MFN and MFNH1 in the voltage range of 4.3 V-1.5 V are shown in Figure 6(d) and 6(e), respectively. For quantitative comparison, the data for y-axis in CV plots are divided by the corresponding activity masses for the cells. In this CV plots, the first oxidation peak at about 3.2 V is mainly contributed by $Ni^{2+/3+}$, and it is also related to the oxidation of a small amount of Fe. This is consistent with other works[45] and has been verified by the soft XAS and XPS results in this work. The second oxidation peak is mainly generated by $Ni^{3+/4+}$. The third peak reflects the oxidation behavior of lattice oxygen. In addition, it is discovered that, at the range of 1.5 V to 2.5 V, the response current of MFNH1 is a little larger than that of MFN, which may be related to the disordered Mn cations. CV results show that the reversibility of redox reaction of oxygen is enhanced, and the stability of transition metal redox

reaction is enhanced.

The Na^+ diffusion coefficient in the cathode can be calculated based on the CV test results with the help of the potentiostatic intermittent titration technique (PITT) test results. The Na^+ diffusion coefficient can be calculated by the following equation.

$$I_p=2.69\times10^5 n^{3/2} A D^{1/2} v^{1/2} \Delta C_0$$

Where I_p is the peak current, n is the number of electrons transferred in the redox reaction (1 for Na^+), A is the area entering the cathode in the electrolyte, D is the Na^+ diffusion coefficient, ΔC_0 is the concentration of Na^+ change, and v is the sweep speed. PITT results reflect the diffusion ability of Na^+, as shown in Figure 6(f) and 6(g). It can be seen that the higher Na ion diffusion coefficient for MFNH1 than MFN is exhibited at the high voltages. This is related to the effect of MFNH1 on the inhibition of structural collapse. And at about 4.1-4.3 V, the Na ion diffusion coefficients experience a sharp reduce, this is related to the oxygen anion redox. In addition, the higher Na ion diffusion coefficient of MFNH1 than MFN at this stage may be related to the inhibition of O-O dimer production.

The electrochemical impedance spectroscope (EIS) results reflect the electrical resistance, R_{ct} and Z_w of two samples were measured by EIS technology in Figure 6(h) and 6(i), which correspond to charge transfer resistance and Na^+ diffusion ability. The results show that the electrochemical impedance of the modified material decreased, and the conductivity enhanced.

2.4. DFT Theoretical Calculation

In order to prove that the Na/Mn anti-site defects can activate the reversible redox

activity of oxygen, first-principle calculations of MFN were carried out. First-principle calculations were performed by the DFT using the vienna ab-initio simulation package (VASP)[60-62]. The detailed calculation methods are given in Supplementary Information. Figure 7(a) shows the DFT calculation models of MFN. The chemical formula of the model is $Na_{26}Mn_1[Mn_8\square_1Fe_9Ni_9]O_{54}$, and a Mn atom replaces a Na atom to produce a TM vacancy. Figure 7(c) shows the calculation results of partial density of states (PDOS) and crystal orbital overlap population (COOP) of MFN. Distribution and arrangement of transition metal *d* electrons at energy levels e_g and t_{2g} (Figure S26) are obtained according to DFT calculation. Combined with PDOS calculation results, the orbital energy band are roughly divided[63]. The Ni^{2+} t_{2g} orbital electrons of are provided by *d* electrons of Ni^{2+}, which tends to form non-bonding state t_{2g} orbitals. In addition, the electrons in the e_g orbital of Ni^{2+} will bond with the electrons in the O 2*p* orbitals to form bonding state e_g and anti-bonding state e_g^*. The energy of electrons in the e_g^* orbit is high, and the electrons will be excited during charging. Therefore, the calculation results show that as for the three transition metals Mn^{4+}, Fe^{3+} and Ni^{2+}, only Ni^{2+} undergoes redox to provide charge compensation ($Ni^{2+} - 2e^- = Ni^{4+}$, $Ni^{4+} + 2e^- = Ni^{2+}$). 0.33 mol Ni^{2+} will provide 0.66 mol electrons and an equivalent specific capacity of about 160 mAh g^{-1}.

DFT calculation results show that the energy band range of -0.61 eV-0 eV is $|O_{2p}$, which proves that MFN material has O redox activity. The band center energy of $|O_{2p}$ is -0.38 eV, and the band energy center of empty Mn e_g^* orbit above Fermi level is 0.68 eV. The charge transfer term required for the electron located in the $|O_{2p}$ orbital to

transfer to the nearest Mn e_g^* orbital above the Fermi level is Δ, Δ = 1.06 eV, as shown in Figure S27. In addition, PDOS diagram shows that a small part of $|O_{2p}$ energy levels are above Ni e_g^*, which indicates that a small part of oxygen has a poor redox reversibility[64, 65]. According to the DFT calculation results and crystal field theory, the diagram of MO_6 coordination orbits of MFN is drawn, as shown in Figure 7(e). O located at the defect provides four electrons to participate in the formation of M-O bond and two electrons to form $|O_{2p}$ orbital in non-bonding state[41].

The above DFT calculation results show that the redox activity and reversibility of oxygen in O3-type MFN material are poor. Therefore, the redox reaction of oxygen is modulated by doping Ho^{3+}. In MFN, 0.01 mol of Ho^{3+} is used to replace 0.01 mol of Fe^{3+}, and the chemical formula is $NaMn_{1/3}Fe_{1/3-0.01}Ni_{1/3}Ho_{0.01}O_2$, which is abbreviated as MFNH1. Figure 7(b) shows the DFT calculation models of MFNH1. The chemical formula of the model is $Na_{25}Mn_2[Mn_7\square_2Fe_8Ho_1Ni_9]O_{54}$, where a Ho atom replaces a Fe atom and two Mn atoms replace two Na atoms to produce two TM vacancies. Figure 7(d) shows the calculation results of partial density of states (PDOS) and crystal orbital overlap population (COOP) of MFNH1. DFT calculation results show that the energy band range of -1.15 eV-0 eV is $|O_{2p}$. The band center energy of $|O_{2p}$ is -0.69 eV. The PDOS results show that Ho^{3+} doping will cause the splitting of TM *3d* orbits energy band, and the energy of the split new Mn e_g^* energy band becomes lower. The band energy center of new Mn e_g^* orbit above Fermi level is 0.17 eV. The charge transfer term required for the electron located in the $|O_{2p}$ orbital to transfer to the nearest Mn e_g^* orbital above the Fermi level is Δ^*, Δ^* = 0.86 eV, which proves that the oxygen

redox activity in MFNH1 is stronger than MFN (Δ = 1.06 eV), as shown in Figure S28. The $|O_{2p}$ energy level is not above the Ni e_g^* energy level, so the oxygen redox has a strong reversibility in MFNH1, which is much better than that of MFN. The above calculated results are consistent with the experimental results of XAS and RIXS. The diagram of MO_6 coordination orbits of MFNH1 is shown in Figure 7(f).

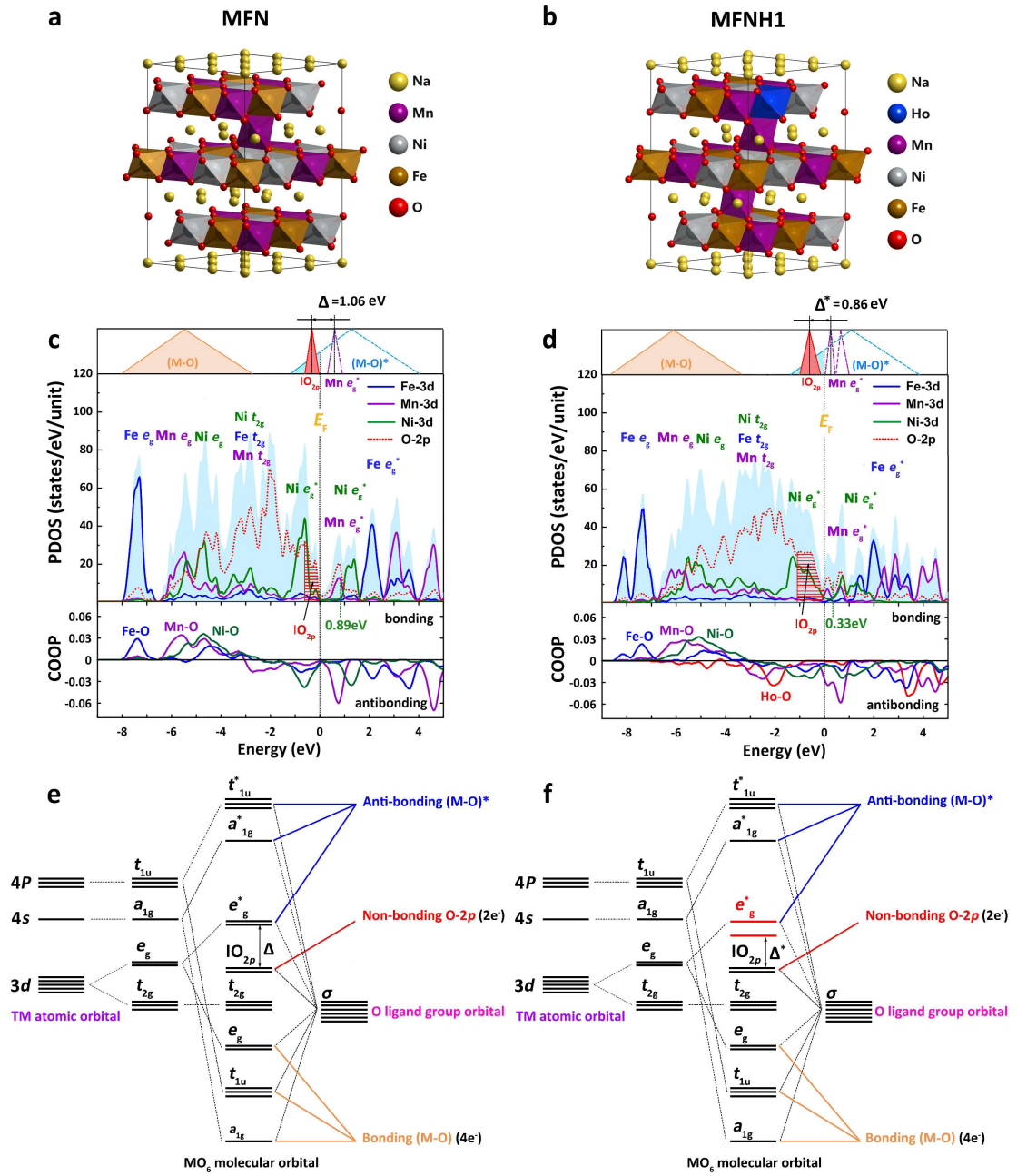

Figure 7. The DFT calculation models of (a) MFN and (b) MFNH1. The calculation

results of PDOS and COOP of (c) MFN and (d) MFNH1. The energy level splitting diagrams of octahedral coordination orbits of (e) MFN and (f) MFNH1.

In addition, the Ni e_g^* orbital band above the Fermi level also splits, the energy of lowest unoccupied molecular orbital (LOMO) of split Ni e_g^* band (0.33 eV, Figure 7(d)) is lower than that of non-split (0.89 eV, Figure 7(c)), which shows that MFNH1 material could have better conductivity and higher redox activity of Ni^{2+}. As a result, according to the calculation results, MFNH1 material should have lower resistance and higher specific capacity. This is consistent with the experimental results of electrochemical performance test.

3. Conclusion

In summary, we clarify that the Na/Mn anti-site defects caused by TM migrations mainly trigger the OAR in O3-type $NaMn_{1/3}Fe_{1/3}Ni_{1/3}O_2$ cathode. OAR activity and reversibility of $NaMn_{1/3}Fe_{1/3}Ni_{1/3}O_2$ cathode is enhanced through tuning Na/Mn anti-site defects with Ho doping. Ho^{3+} doping not only modulates the formation of Na/Mn anti-site defects to enhance the degree of oxygen participating in redox reaction but also adjusts the bond length and bond angle to improve the reversibility of oxygen redox. At the same time, TM *3d* orbits energy band splitting induced by Ho^{3+} doping activates the redox activity of both anion and cation. In addition, Mn^{2+} pinning effect and the strong Ho-O bond inhibit the excessive phase transition and enhance the crystal structural stability. After doping 0.01 mol Ho^{3+} at Fe^{3+} site, the specific capacity is increased from 146.8 to 184.9 mAh g^{-1}, and the capacity retention rate after 100 cycles at 5 C is increased from 40.3% to 90.0%. This work reveals the redox process and

mechanism of oxygen in O3-type (sodium-full) cathodes and provides new insights in modulating the oxygen redox chemistry for high-performance cathode materials.

Associated Content

Supplementary Information Available: Experimental Section, NPD, XRD Rietveld refinement result and atomic site occupation data, and ICP analysis data. PDOS results, XAS spectra, EXAFS spectra, XPS spectra, Raman results, HR-TEM images, TEM-EDS mapping, SEM images, ex-situ EPR results and electrochemical performance diagram.

Acknowledgements

This work was supported by National Natural Science Foundation of China (Grant No. 11975238, 11575192 and 11675267), the Chinese Academy of Sciences (Grant No. ZDKYYQ20170001, 211211KYSB20170060 and 211211KYSB20180020) and Natural Science Foundation of Beijing Municipality (Grant No. 2182082). This work was also supported by the Fundamental Research Funds for the Central Universities. The support from University of Chinese Academy of Sciences is also appreciated. The present research used resources at the SNS, a U.S. Department of Energy (DOE) Office of Science User Facility operated by the ORNL.

References

1. N. Yabuuchi, K. Kubota, M. Dahbi and S. Komaba, *Chemical Reviews*, 2014, **114**, 11636-11682.
2. J.-Y. Hwang, S.-T. Myung and Y.-K. Sun, *Chemical Society Reviews*, 2017, **46**, 3529-3614.
3. H. Pan, Y.-S. Hu and L. Chen, *Energy & Environmental Science*, 2013, **6**, 2338-

2360.

4. D. Kundu, E. Talaie, V. Duffort and L. F. Nazar, *Angewandte Chemie International Edition*, 2015, **54**, 3431-3448.

5. P. K. Nayak, L. Yang, W. Brehm and P. Adelhelm, *Angewandte Chemie International Edition*, 2018, **57**, 102-120.

6. M. H. Han, E. Gonzalo, G. Singh and T. Rojo, *Energy & Environmental Science*, 2015, **8**, 81-102.

7. N. Ortiz-Vitoriano, N. E. Drewett, E. Gonzalo and T. Rojo, *Energy & Environmental Science*, 2017, **10**, 1051-1074.

8. V. Palomares, M. Casas-Cabanas, E. Castillo-Martínez, M. H. Han and T. Rojo, *Energy & Environmental Science*, 2013, **6**, 2312-2337.

9. G.-L. Xu, R. Amine, Y.-F. Xu, J. Liu, J. Gim, T. Ma, Y. Ren, C.-J. Sun, Y. Liu, X. Zhang, S. M. Heald, A. Solhy, I. Saadoune, W. L. Mattis, S.-G. Sun, Z. Chen and K. Amine, *Energy & Environmental Science*, 2017, **10**, 1677-1693.

10. S.-W. Kim, D.-H. Seo, X. Ma, G. Ceder and K. Kang, *Advanced Energy Materials*, 2012, **2**, 710-721.

11. Y. You and A. Manthiram, *Advanced Energy Materials*, 2018, **8**, 1701785.

12. H. Kim, H. Kim, Z. Ding, M. H. Lee, K. Lim, G. Yoon and K. Kang, *Advanced Energy Materials*, 2016, **6**, 1600943.

13. R.-M. Gao, Z.-J. Zheng, P.-F. Wang, C.-Y. Wang, H. Ye and F.-F. Cao, *Energy Storage Materials*, 2020, **30**, 9-26.

14. Y.-F. Zhu, Y. Xiao, S.-X. Dou, Y.-M. Kang, S.-L. Chu, *eScience*, 2021, **1**, 13-27.

15. G. Assat and J.-M. Tarascon, *Nature Energy*, 2018, **3**, 373-386.

16. N. Yabuuchi, R. Hara, M. Kajiyama, K. Kubota, T. Ishigaki, A. Hoshikawa and S. Komaba, *Advanced Energy Materials*, 2014, **4**, 1301453.

17. K. Du, J. Zhu, G. Hu, H. Gao, Y. Li and J. B. Goodenough, *Energy & Environmental Science*, 2016, **9**, 2575-2577.

18. X. Rong, J. Liu, E. Hu, Y. Liu, Y. Wang, J. Wu, X. Yu, K. Page, Y.-S. Hu, W. Yang, H. Li, X.-Q. Yang, L. Chen and X. Huang, *Joule*, 2018, **2**, 125-140.

19. E. de la Llave, E. Talaie, E. Levi, P. K. Nayak, M. Dixit, P. T. Rao, P. Hartmann, F. Chesneau, D. T. Major, M. Greenstein, D. Aurbach and L. F. Nazar, *Chemistry of Materials*, 2016, **28**, 9064-9076.
20. X. Rong, E. Hu, Y. Lu, F. Meng, C. Zhao, X. Wang, Q. Zhang, X. Yu, L. Gu, Y.-S. Hu, H. Li, X. Huang, X.-Q. Yang, C. Delmas and L. Chen, *Joule*, 2019, **3**, 503-517.
21. N. Yabuuchi, R. Hara, K. Kubota, J. Paulsen, S. Kumakura and S. Komaba, *Journal of Materials Chemistry A*, 2014, **2**, 16851-16855.
22. K. Dai, J. Wu, Z. Zhuo, Q. Li, S. Sallis, J. Mao, G. Ai, C. Sun, Z. Li, W. E. Gent, W. C. Chueh, Y.-d. Chuang, R. Zeng, Z.-x. Shen, F. Pan, S. Yan, L. F. J. Piper, Z. Hussain, G. Liu and W. Yang, *Joule*, 2019, **3**, 518-541.
23. X. Bai, M. Sathiya, B. Mendoza-Sánchez, A. Iadecola, J. Vergnet, R. Dedryvère, M. Saubanère, A. M. Abakumov, P. Rozier and J.-M. Tarascon, *Advanced Energy Materials*, 2018, **8**, 1802379.
24. B. Mortemard de Boisse, S.-i. Nishimura, E. Watanabe, L. Lander, A. Tsuchimoto, J. Kikkawa, E. Kobayashi, D. Asakura, M. Okubo and A. Yamada, *Advanced Energy Materials*, 2018, **8**, 1800409.
25. B. Mortemard de Boisse, G. Liu, J. Ma, S.-i. Nishimura, S.-C. Chung, H. Kiuchi, Y. Harada, J. Kikkawa, Y. Kobayashi, M. Okubo and A. Yamada, *Nature Communications*, 2016, **7**, 11397.
26. A. J. Perez, D. Batuk, M. Saubanère, G. Rousse, D. Foix, E. McCalla, E. J. Berg, R. Dugas, K. H. W. van den Bos, M.-L. Doublet, D. Gonbeau, A. M. Abakumov, G. Van Tendeloo and J.-M. Tarascon, *Chemistry of Materials*, 2016, **28**, 8278-8288.
27. P. E. Pearce, G. Rousse, O. M. Karakulina, J. Hadermann, G. Van Tendeloo, D. Foix, F. Fauth, A. M. Abakumov and J.-M. Tarascon, *Chemistry of Materials*, 2018, **30**, 3285-3293.
28. P. Rozier, M. Sathiya, A.-R. Paulraj, D. Foix, T. Desaunay, P.-L. Taberna, P. Simon and J.-M. Tarascon, *Electrochemistry Communications*, 2015, **53**, 29-32.

29. Y.-K. Sun, *ACS Energy Letters*, 2020, **5**, 1278-1280.
30. Q. Liu, Z. Hu, W. Li, C. Zou, H. Jin, S. Wang, S. Chou and S.-X. Dou, *Energy & Environmental Science*, 2021, **14**, 158-179.
31. N. Voronina and S.-T. Myung, *Energy Material Advances*, 2021, **2021**, 9819521.
32. Y. Yu, D. Ning, Q. Li, A. Franz, L. Zheng, N. Zhang, G. Ren, G. Schumacher and X. Liu, *Energy Storage Materials*, 2021, **38**, 130-140.
33. K. An, Y. Chen and A. D. Stoica, *MRS Bulletin*, 2019, **44**, 878-885.
34. C. Schulz, K. Lieutenant, J. Xiao, T. Hofmann, D. Wong and K. Habicht, *Journal of Synchrotron Radiation*, 2020, **27**, 238-249.
35. W. K. Pang, S. Kalluri, V. K. Peterson, N. Sharma, J. Kimpton, B. Johannessen, H. K. Liu, S. X. Dou and Z. Guo, *Chemistry of Materials*, 2015, **27**, 3150-3158.
36. N. Jiang, Q. Liu, J. Wang, W. Yang, W. Ma, L. Zhang, Z. Peng and Z. Zhang, *Small*, 2021, **17**, 2007103.
37. Y.-J. Guo, P.-F. Wang, Y.-B. Niu, X.-D. Zhang, Q. Li, X. Yu, M. Fan, W.-P. Chen, Y. Yu, X. Liu, Q. Meng, S. Xin, Y.-X. Yin and Y.-G. Guo, *Nature Communications*, 2021, **12**, 5267.
38. A. Rougier, C. Delmas and A. V. Chadwick, *Solid State Communications*, 1995, **94**, 123-127.
39. J.-P. Ma, Y.-M. Chen, L.-M. Zhang, S.-Q. Guo, J.-D. Liu, H. Li, B.-J. Ye, Z.-Y. Li, Y. Zhou, B.-B. Zhang, O. M. Bakr, J.-Y. Zhang and H.-T. Sun, *Journal of Materials Chemistry C*, 2019, **7**, 3037-3048.
40. J.-K. Chen, J.-P. Ma, S.-Q. Guo, Y.-M. Chen, Q. Zhao, B.-B. Zhang, Z.-Y. Li, Y. Zhou, J. Hou, Y. Kuroiwa, C. Moriyoshi, O. M. Bakr, J. Zhang and H.-T. Sun, *Chemistry of Materials*, 2019, **31**, 3974-3983.
41. M. Okubo and A. Yamada, *ACS Applied Materials & Interfaces*, 2017, **9**, 36463-36472.
42. H. Xu, S. Guo and H. Zhou, *Journal of Materials Chemistry A*, 2019, **7**, 23662-23678.
43. H. Ren, Y. Li, Q. Ni, Y. Bai, H. Zhao and C. Wu, *Advanced Materials*, 2022, **34**,

2106171.

44. Q. Li, D. Zhou, L. Zhang, D. Ning, Z. Chen, Z. Xu, R. Gao, X. Liu, D. Xie, G. Schumacher and X. Liu, *Advanced Functional Materials*, 2019, **29**, 1806706.

45. R. A. House, U. Maitra, M. A. Pérez-Osorio, J. G. Lozano, L. Jin, J. W. Somerville, L. C. Duda, A. Nag, A. Walters, K.-J. Zhou, M. R. Roberts and P. G. Bruce, *Nature*, 2020, **577**, 502-508.

46. U. Maitra, R. A. House, J. W. Somerville, N. Tapia-Ruiz, J. G. Lozano, N. Guerrini, R. Hao, K. Luo, L. Jin, M. A. Pérez-Osorio, F. Massel, D. M. Pickup, S. Ramos, X. Lu, D. E. McNally, A. V. Chadwick, F. Giustino, T. Schmitt, L. C. Duda, M. R. Roberts and P. G. Bruce, *Nature Chemistry*, 2018, **10**, 288-295.

47. S. Erat, A. Braun, A. Ovalle, C. Piamonteze, Z. Liu, T. Graule and L. J. Gauckler, *Applied Physics Letters*, 2009, **95**, 174108.

48. Y. Xie, H. Wang, G. Xu, J. Wang, H. Sheng, Z. Chen, Y. Ren, C.-J. Sun, J. Wen, J. Wang, D. J. Miller, J. Lu, K. Amine and Z.-F. Ma, *Advanced Energy Materials*, 2016, **6**, 1601306.

49. S. Chu, C. Zhang, H. Xu, S. Guo, P. Wang and H. Zhou, *Angewandte Chemie International Edition*, 2021, **60**, 13366-13371.

50. W. Kong, R. Gao, Q. Li, W. Yang, J. Yang, L. Sun and X. Liu, *Journal of Materials Chemistry A*, 2019, **7**, 9099-9109.

51. W. Kong, H. Wang, Y. Zhai, L. Sun and X. Liu, *The Journal of Physical Chemistry C*, 2018, **122**, 25909-25916.

52. W. Yang and T. P. Devereaux, *Journal of Power Sources*, 2018, **389**, 188-197.

53. J.-N. Zhang, Q. Li, C. Ouyang, X. Yu, M. Ge, X. Huang, E. Hu, C. Ma, S. Li, R. Xiao, W. Yang, Y. Chu, Y. Liu, H. Yu, X.-Q. Yang, X. Huang, L. Chen and H. Li, *Nature Energy*, 2019, **4**, 594-603.

54. Q. Li, D. Ning, D. Zhou, K. An, D. Wong, L. Zhang, Z. Chen, G. Schuck, C. Schulz, Z. Xu, G. Schumacher and X. Liu, *Journal of Materials Chemistry A*, 2020, **8**, 7733-7745.

55. J. Zhang, Q. Zhang, D. Wong, N. Zhang, G. Ren, L. Gu, C. Schulz, L. He, Y. Yu

and X. Liu, *Nature Communications*, 2021, **12**, 3071.

56. A. Tsuchimoto, X.-M. Shi, K. Kawai, B. Mortemard de Boisse, J. Kikkawa, D. Asakura, M. Okubo and A. Yamada, *Nature Communications*, 2021, **12**, 631.

57. X. Zhang, Y. Qiao, S. Guo, K. Jiang, S. Xu, H. Xu, P. Wang, P. He and H. Zhou, *Advanced Materials*, 2019, **31**, 1807770.

58. Y. Qiao, S. Guo, K. Zhu, P. Liu, X. Li, K. Jiang, C.-J. Sun, M. Chen and H. Zhou, *Energy & Environmental Science*, 2018, **11**, 299-305.

59. R. A. House, G. J. Rees, M. A. Pérez-Osorio, J.-J. Marie, E. Boivin, A. W. Robertson, A. Nag, M. Garcia-Fernandez, K.-J. Zhou and P. G. Bruce, *Nature Energy*, 2020, **5**, 777-785.

60. G. Kresse and J. Furthmüller, *Computational Materials Science*, 1996, **6**, 15-50.

61. J. P. Perdew, K. Burke and M. Ernzerhof, *Physical Review Letters*, 1996, **77**, 3865-3868.

62. M. H. N. Assadi and Y. Shigeta, *RSC Advances*, 2018, **8**, 13842-13849.

63. C. Zhao, Z. Yao, Q. Wang, H. Li, J. Wang, M. Liu, S. Ganapathy, Y. Lu, J. Cabana, B. Li, X. Bai, A. Aspuru-Guzik, M. Wagemaker, L. Chen and Y.-S. Hu, *Journal of the American Chemical Society*, 2020, **142**, 5742-5750.

64. M. Ben Yahia, J. Vergnet, M. Saubanère and M.-L. Doublet, *Nature Materials*, 2019, **18**, 496-502.

65. M. Saubanère, E. McCalla, J. M. Tarascon and M. L. Doublet, *Energy & Environmental Science*, 2016, **9**, 984-991.